BIOCHEMISTRY
including biophysical chemistry & molecular biology

Article

pubs.acs.org/biochemistry

Structural and Biophysical Insights into the Ligand-Free Pitx2 Homeodomain and a Ring Dermoid of the Cornea Inducing Homeodomain Mutant

Thomas Doerdelmann,[†] Douglas J. Kojetin,[†,‡] Jamie M. Baird-Titus,[§] Laura A. Solt,[‡] Thomas P. Burris,[‡] and Mark Rance*[,†]

[†]Department of Molecular Genetics, Biochemistry and Microbiology, University of Cincinnati, 231 Albert Sabin Way, Cincinnati, Ohio 45267, United States

[‡]Department of Molecular Therapeutics, Scripps Florida, The Scripps Research Institute, 130 Scripps Way, Jupiter, Florida 33458, United States

[§]Department of Chemistry, College of Mount St. Joseph, 5701 Delhi Road, Cincinnati, Ohio 45233, United States

Supporting Information

ABSTRACT: The homeodomain-containing transcription factor Pitx2 (pituitary homeobox protein 2) is present in many developing embryonic tissues, including the heart. Its homeodomain is responsible for the recognition and binding to target DNA sequences and thus constitutes a major functional unit in the Pitx2 protein. Nuclear magnetic resonance techniques were employed to determine the solution structure of the native Pitx2 homeodomain and a R24H mutant that causes autosomal dominantly inherited ring dermoid of the cornea syndrome. The structures reveal that both isoforms possess the canonical homeodomain fold. However, the R24H mutation results in a 2-fold increase in DNA binding affinity and a 5 °C decrease in thermal stability, while changing the dynamic environment of the homeodomain only locally. When introduced into full-length Pitx2c, the mutation results in an only 25% loss of transactivation activity. Our data correlate well with clinical observations suggesting a milder deficiency for the R24H mutation compared to those of other Pitx2 homeodomain mutations.

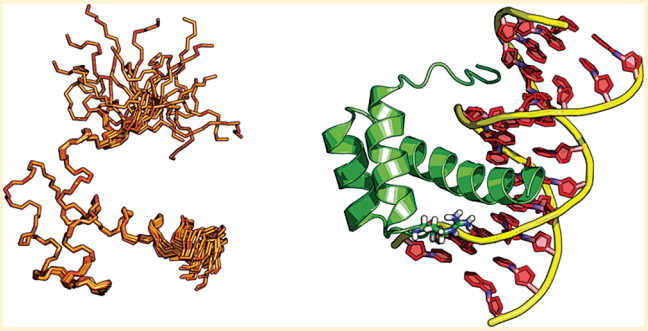

The homeodomain-containing pituitary homeobox 2 (Pitx2) protein is a pivotal transcription factor required for the development of embryonic left−right asymmetry, as well as maintenance of several adult tissues, including the pituitary, eye, and heart.[1−10] In humans, haploinsufficiency of the Pitx2 allele (through absence or mutation) causes a range of developmental disorders and disease states, ranging from developmental syndromes like Axenfeld-Rieger to glaucoma.[8,11−13] Loss of PITX2 function in mice is lethal and causes severe cardiovascular defects such as atrial isomerism, double inlet left ventricle, transposition of the great arteries, persistent truncus arteriosus, and abnormal aortic arch remodeling.[14] Consistent with the severity of Pitx2 phenotypes, it has been shown to be a central downstream transcriptional activator in the canonical WNT/β-catenin signaling pathway[15,16] and plays an important role in TGF-β signaling.[17−20]

The homeodomain is an evolutionarily conserved protein fold present in transcription factors. Given the high frequency of the homeodomain, it has served as a model system for probing the functional and structural aspects of protein−DNA interactions over the past two decades.[21−39] The 60-amino acid homeodomain, canonically numbered 1−60, contains a helix−turn−helix motif that binds both DNA and RNA in prokaryotic and eukaryotic organisms (Figure 1).[40] The tertiary structure consists of three helical regions folded into a compact, globular structure with an N-terminal extension. Helix 1 (α1) is preceded by the N-terminal arm and is separated by a loose loop from the helix−turn−helix motif formed by helices 2 (α2) and 3 (α3) (Figure 2A). Helix 3, also called the recognition helix, lies in the major groove of the DNA and establishes specific contacts with the DNA bases. The N-terminal arm makes additional contacts with the bases in the DNA minor groove. In addition to the recognition helix and the N-terminal arm, the loop between α1 and α2 also interacts with the DNA backbone.[21,24] Typically, eight highly conserved hydrophobic amino acids (in the Pitx2 homeodomain, they are F8, L13, L16, F20, L40, V45, W48, and F49) spread throughout the three helices constitute the hydrophobic protein core.[24]

The homeodomain that is present in three of four characterized Pitx2 isoforms has been identified as a hotspot

Received: October 28, 2011
Revised: December 20, 2011
Published: December 21, 2011

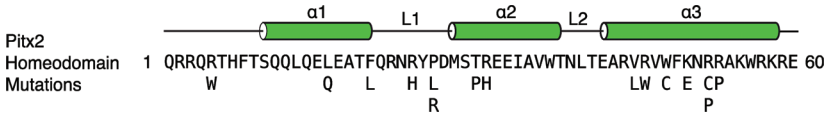

Figure 1. Human Pitx2 homeodomain amino acid sequence, secondary structure elements, and reported missense mutations. The numbering of the consensus sequence runs from 1 to 60. Mutations were compiled from refs 8, 11−13, and 41−49.

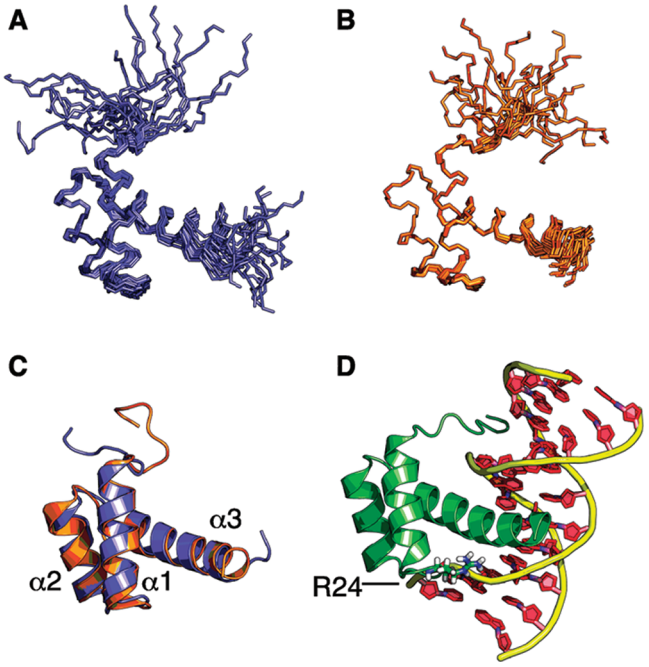

Figure 2. Ribbon and cartoon representations of the Pitx2 homeodomain solution structures. Ensemble of the 20 lowest-energy structures for (A) the wild-type Pitx2 homeodomain (PDB entry 2L7F) and (B) the R24H mutant Pitx2 homeodomain (PDB entry 2L7M). (C) Maximum likelihood superposition of closest to the average wild-type (blue) and R24H (orange) structures. (D) Structure of the Pitx2 homeodomain−TAATCC consensus DNA complex[24] (PDB entry 2lkx). Residue 24 is located in the loop connecting helices 1 and 2.

for mutations. Of the known disease-causing missense mutations, the majority can be found in the homeodomain (Figure 1).[8,11−13,41−49] The majority of these homeodomain mutations fall into three broad categories: (1) modifying DNA binding ability, (2) enhancing or diminishing transactivation capability, and (3) having an impact on protein stability. One such mutation that displays mild characteristics of all three categories, as we determined here, involves an amino acid substitution at position 24 of the homeodomain. This arginine to histidine substitution (R24H) corresponds to position 62 in Pitx2a, position 108 in Pitx2b, and position 115 in Pitx2c and results in autosomal dominantly inherited ring dermoid of the cornea syndrome.[41] Unlike many other Pitx2 homeodomain mutations, the only clinical manifestations in R24H-affected patients are in the eyes,[41] suggesting that from a clinical perspective this may be considered a mild mutation.

To characterize the effects of the R24H mutation in the Pitx2 homeodomain and to provide some insight into the origin of the clinical manifestations of this mutation, we have performed an in-depth characterization of the structure, dynamics, and functional properties of both the wild-type and R24H mutant homeodomains. The combined results of the NMR structure determinations, dynamics measurements, and other biophysical and functional studies indicate that for the most part the perturbations introduced by the R24H mutation are generally modest and impart mild changes in DNA binding affinity, transactivation activity, and conformational stability compared to those of wild-type Pitx2.

MATERIALS AND METHODS

Protein Expression and Purification. Proteins were expressed from a pet28 expression vector as a His_6-TEV-GS-Pitx2 homeodomain-EFIVTD fusion protein in *Escherichia coli* BL21DE3star cells (Invitrogen). Expression conditions were as described previously.[24] Cells were harvested by centrifugation at 2500*g* for 15 min. Harvested cells were resuspended in 137 mM NaCl, 2.7 mM KCl, 10 mM sodium phosphate dibasic, and 2 mM potassium phosphate monobasic (pH 7.4) (PBS) with the addition of 10 mM imidazole. Resuspended cells were lysed by being passed through a chilled French press twice at 12000 psi. The lysate was cleared by centrifugation at 25000*g* for 30 min at 4 °C. The cleared lysate was applied to a pre-equilibrated 5 mL HisTrap HP column (GE Lifesciences). The column was washed with 10 column volumes (cv) of PBS and 10 mM imidazole. Next, an additional wash step of 10 cv with PBS and 100 mM imidazole was performed. The target fusion protein was eluted with 10 cv of PBS and 500 mM imidazole. Protein concentrations were estimated via A_{278} (ε_{278} = 18350 cm^{-1} M^{-1}), and the eluate was adjusted to contain 10% (v/v) glycerol, 5 mM β-mercaptoethanol, and 5 mM EDTA. TEV protease produced in house was added for fusion tag removal at a 1:25 ratio, and cleavage was performed at 4 °C over 4 h. Cleaved protein was then loaded on a 1 mL HiTrap SP FF (GE Lifesciences) cation exchange column, washed with washing buffer [10 mM NaH_2PO_4 and 400 mM NaCl (pH 7.0)], and eluted with buffer containing a higher salt concentration [10 mM NaH_2PO_4 and 1 M NaCl (pH 7.0)]. Purity was determined to be >98% by sodium dodecyl sulfate−polyacrylamide gel electrophoresis (SDS−PAGE). The eluted homeodomain was then dialyzed overnight at 4 °C into 10 mM NaH_2PO_4, 150 mM Na_2SO_4, and 1 mM EDTA (pH 7.0) for NMR or as indicated for the biophysical experiments. Proteins were then concentrated utilizing Amicon Ultra15 spin filters (Millipore) with a molecular cutoff of 3 kDa.

Consensus Response Element DNA. All DNA was purchased from IDTDNA. The utilized constructs were sense 5′-GCTCTAATCCCCG-3′ and antisense 3′-CGAGAT-TAGGGGC-5′ with the complex termed TAATCC or consensus DNA. To obtain double-stranded DNA, we annealed the cDNA strands by heating them for 15 min at 95 °C followed by rapid cooling on ice.

Nuclear Magnetic Resonance Spectroscopy and Structural Calculations. For the structural studies, NMR sample concentrations ranged from approximately 0.25 to 1.5 mM, in 90% 10 mM NaH_2PO_4, 150 mM Na_2SO_4 (pH 7.0), and 10% D_2O. All NMR experiments were conducted on Varian Inova 400, 500, 600, and 800 MHz spectrometers. The sample temperature was set to 295 K, and spectra were referenced to

dx.doi.org/10.1021/bi201639x | *Biochemistry* 2012, 51, 665−676

an external DSS standard. Standard triple-resonance methodology using protein that was uniformly labeled with ^{13}C and ^{15}N was employed as described previously.[21,24] Raw data were processed utilizing NMRPipe,[50] and spectra were analyzed via NMRViewJ.[51] Dihedral angles were predicted utilizing Talos +,[52] and only good predictions were utilized during structure calculations. CYANA structures were calculated as previously described.[21,24] One hundred final cycle CYANA structures were subsequently refined using the generalized Born potential[53] implemented in AMBER 10[54] to account for solvent effects as previously detailed.[55] Twenty structures were determined by FINDFAM[56] to be sufficient to represent the conformational space consistent with the experimental data and were used to represent the NMR structure ensemble. The quality of the final NMR structures was assessed utilizing MolProbity.[57]

For the histidine side chain pH titrations, a ^{15}N-labeled sample was prepared at pH 4.0 as described above. Utilizing $^{1}H-^{15}N$ multiple-bond correlation experiments,[58] chemical shift values were measured in 0.5 pH unit increments. To calculate pK_a values, the pH dependencies of the chemical shifts were fitted by nonlinear regression to the Henderson–Hasselbalch equation (eq 1) utilizing GraphPad Prism.

$$\delta = \delta_0 + \frac{\Delta\delta}{1 + 10^{\mathrm{pH}-\mathrm{p}K_a}} \quad (1)$$

where δ is the measured chemical shift, δ_0 is the chemical shift of the deprotonated form, and $\Delta\delta$ is the difference between the protonated and deprotonated forms.

Collection and Analysis of ^{15}N Backbone Relaxation Data. Relaxation data for the wild-type Pitx2 homeodomain were recorded using a 0.5 mM sample. For the R24H mutant homeodomain, data were collected for four samples generated by serial dilutions, with concentrations of 1, 0.5, 0.25, and 0.125 mM. Backbone ^{15}N relaxation rate constants R_1 and R_2 were determined from data recorded at 400 and 600 MHz, and $\{^{1}H\}-^{15}N$ heteronuclear NOE values were determined from data recorded at 600 MHz via sensitivity-enhanced pulse sequences.[59,60] The R_1 and R_2 experiments did not employ a water flip-back scheme, whereas the NOE experiment did. The R_2 measurements were made using a CPMG pulse train with a pulse spacing of 1 ms (center to center) and radiofrequency field strengths of 5 kHz (600 MHz data) and 4.2 kHz (400 MHz data); to avoid possible sample heating effects from the CPMG pulse train,[61,62] the delay between transients was set to 3 s and a constant duty cycle for the ^{15}N irradiation was achieved by including a second CPMG block at the beginning of the pulse sequence that was adjusted such that the sum of the two CPMG blocks was a constant.[63] For the R_1 and R_2 experiments, the data for the various time points were collected in an interleaved fashion, the peak intensities were quantitated using the autoFit software in the NMRPipe package, and errors in intensities were determined from a combination of repeat measurements for several time points and evaluation of the baseplane noise. The rate constants and associated errors were determined using Curvefit.[64] The NOE values were determined from pairs of two-dimensional (2D) spectra; in one case (NOE spectrum), a train of 180° ^{1}H pulses separated by 50 ms was applied[65] for a duration of 4 s at the beginning of the pulse sequence, and in the other case (reference spectrum), the same ^{1}H pulse train was applied but with the power level at the minimal hardware setting and with the frequency shifted far off-resonance. For the reference spectrum, an additional 2 s was included in the recovery period between transients, for a total recycle delay of 6 s. The NOE and reference data sets were recorded in an interleaved fashion to minimize systematic errors. Three repeats of the NOE measurement were performed, and the results were averaged together.

Generalized order parameters, S^2, were determined from the ^{15}N R_1 and R_2 relaxation rate constants at 400 and 600 MHz and the 600 MHz $\{^{1}H\}-^{15}N$ heteronuclear NOE using Modelfree (version 4.20)[64] and a protocol similar to that reported previously.[66] Three dynamical models, described previously, were utilized in the data analysis. Using the common nomenclature, these were models 2, 4, and 5. In model 2, S^2 is optimized along with an effective internal correlation time, τ_e. For model 4, a chemical exchange term, R_{ex}, is added to the model 2 parameters. Model 5 attempts to fit the data with two order parameters S_f^2 and S_s^2 ($S^2 = S_f^2 S_s^2$) and one internal correlation time τ_s corresponding to the slower time scale reported on by S_s^2. Initial estimates of the overall rotational diffusion tensor were determined from extensive grid searches for both an isotropic diffusion model and an axially symmetric model. Subsequently, the diffusion tensor parameters were optimized as part of the Modelfree analysis protocol. In the case of the axial diffusion model, one structure from the final ensemble of the 20 lowest-energy structures was selected using THESEUS,[67] which uses a maximum likelihood method to superposition the ensemble and to select the structure closest to the "average" structure for a family.

Circular Dichroism (CD) Spectroscopy. CD experiments were performed on an AVIV 215 CD spectrophotometer. Thermal melts were recorded in 1 °C increments with 3 min equilibration times at 5 μM concentrations in a 1 cm path-length cell under 30 rpm stirring in PBS buffer (pH 7.4) with 5 s signal averaging. Spectra were collected offset (226 nm) from the α-helical minimum (222 nm) as the DNA signal at this wavelength was stable over the temperature range studied. Data analysis was performed as described previously.[68,69]

Isothermal Titration Calorimetry (ITC). Measurements were performed in triplicate in 50 mM NaH_2PO_4 and 150 mM NaCl (pH 7.0) at 25 °C using a MicroCal VP-ITC instrument. Protein concentrations ranged from 10 to 30 μM with a fixed dsDNA concentration of 100 or 300 μM. All DNA and protein samples were buffer matched, and the heat of dilution was measured in a separate experiment and corrected for. Raw data were analyzed assuming a single-binding site model utilizing MicroCal ORIGIN 7.

Luciferase Reporter Transactivation Assay. The cyclin D2 luciferase reporter construct contained 798 bp (−1 to −798) of the cyclin D2 promoter in a pGL4.24 luciferase vector (Promega, Madison, WI).[70] The PITX2c expression construct was situated within a pEGFP-N1 vector (Clontech) expressing N-terminally flag-tagged Pitx2c protein.[70,71] Both vectors were generous gifts of G.-Z. Zhu (Marshall University, Huntington, WV). The R24H mutant was generated using a standard site-directed mutagenesis protocol. Twenty-four hours prior to transfection, HEK293 cells were plated in 96-well plates at a density of 2×10^4 cells/well. A total of 100 ng of reporter and Pitx2 plasmid mixes were transfected into HEK293 cells with Lipofectamine transfection reagent (Invitrogen). Twenty-four or forty-eight hours post-transfection, the luciferase activity was measured using the Dual-Glo luciferase assay system (Promega). Results were analyzed using GraphPad Prism. An empty vector control was performed, and all values were

Table 1. Structural Statistics for the Pitx2 Homeodomain Structure Ensembles (n = 20)

	wild type	R24H mutant
no. of NMR constraints		
distance total	871	1467
intraresidue ($i = j$)	253	402
sequential ($\|i - j\| = 1$)	229	376
medium-range ($1 < \|i - j\| \leq 4$)	263	420
long-range ($\|i - j\| \geq 5$)	126	269
dihedral angles (φ and ψ)	80	98
Amber constraint violations		
average no. of distance constraint violations per structure		
0.1 Å < d < 0.2 Å	0	0.25
d > 0.2 Å	0	0
maximal average distance violation (Å)	0.093	0.156
average no. of dihedral angle violations per structure (θ > 0°)	0	0
maximal average dihedral angle violation (deg)	0	0
ensemble superposition statistics (Å)[a]		
all (residues 1−60)		
backbone atoms	8.34 ± 0.23 (3.32)	4.47 ± 0.05 (1.78)
heavy atoms	8.43 ± 0.29 (3.36)	4.44 ± 0.06 (1.77)
well-ordered regions (residues 8−58)		
backbone atoms	1.33 ± 0.20 (0.53)	0.61 ± 0.05 (0.24)
heavy atoms	1.89 ± 0.24 (0.75)	1.01 ± 0.05 (0.40)
AMBER energies (kcal/mol)		
constraint	1.320 ± 0.132	5.036 ± 0.269
van der Waals	−499.1 ± 9.2	−502.4 ± 6.6
total	−4316.4 ± 16.5	−4095.4 ± 12.2
MolProbity statistics[b]		
MolProbity score	1.20 ± 0.30	1.16 ± 0.15
MolProbity percentile rank	97.70 ± 3.24	99.10 ± 1.18
clash score	0.21 ± 0.36	0.09 ± 0.26
clash score percentile	99.75 ± 0.43	99.90 ± 0.30
Ramachandran space (%)		
favored	96.31 ± 2.68	98.44 ± 1.31
allowed	2.69 ± 2.06	1.09 ± 1.22
outliers	1.00 ± 1.22	0.47 ± 0.72

[a]Ensemble superposition statistics were calculated using THESEUS, reported as classical least-squares pairwise ⟨rmsd⟩ ± ML⟨σ⟩ (LS⟨σ⟩). [b]The MolProbity clash score is the number of serious steric overlaps (>0.4 Å) per 1000 atoms. For the clash score percentile, 100 is the best among structures of comparable resolution and 0 is the worst.

normalized to the luciferase expression from the wild-type reporter to produce fold induction values.

Western Analysis. Twenty-four hours prior to transfection, HEK293 cells were plated in six-well plates at a density of 5 × 10^4 HEK293 cells/well. Transfections were performed using Lipofectamine 2000 (Invitrogen). Twenty-four hours post-transfection, HEK293 cells were washed once with phosphate-buffered saline and then incubated for 10 min at 4 °C in 100 μL of TNT lysis buffer [50 mM Tris-HCl (pH 7.5), 150 mM NaCl, and 1% Triton X-100] and a complete miniprotease inhibitor mixture (Roche Applied Science). Samples were then harvested into 1.5 mL microcentrifuge tubes, vortexed for 30 s, and then centrifuged. Protein levels in the supernatants were determined using a Coomassie protein assay kit (Bio-Rad, Hercules, CA), and 10 μg of protein from each sample was separated by 10% SDS−PAGE (Bio-Rad) and then transferred to a polyvinylidene difluoride membrane (Millipore) and immunoblotted with primary antibodies: α-Flag (Sigma, St. Louis, MO) or α-tubulin (Sigma) and horseradish peroxidase-conjugated secondary antibodies (Jackson Immunoresearch). Detection of the bound antibody by enhanced chemiluminescence was performed according to the manufacturer's instructions (Santa Cruz Biotechnology, Santa Cruz, CA).

RESULTS

NMR Solution Structures of Wild-Type and R24H Mutant Pitx2 Homeodomains. Analysis of ^{15}N and ^{13}C heteronuclear-edited NOESY spectra yielded a total of 871 protein distance restraints for the wild-type and 1467 restraints for the R24H mutant protein (Table 1). On average, there were 13 and 22 nuclear Overhauser effect (NOE) restraints per residue for wild-type and R24H mutant proteins, respectively. The large difference in the number of NOE constraints between the two forms of the homeodomain is due to a factor of 4 difference in the sample concentration employed for the NOE-based experiments and, secondarily, the fact that one of the NOE experiments for the wild-type protein was conducted at 600 MHz on a conventional probe, whereas all of the NOE data for the R24H mutant were collected at 800 MHz using a cryoprobe. NOE and TALOS-predicted dihedral angle restraints were utilized for subsequent CYANA structure calculations. One hundred CYANA structures were subsequently refined in AMBER, and the NMR structural ensemble

consisting of the 20 lowest-energy structures exhibited mean AMBER energies of −4316 kcal/mol for the wild type and −4095 kcal/mol for the mutant protein. When superimposed, the ensemble of the 20 lowest-energy NMR structures exhibited backbone average root-mean-square deviations (rmsds) of 1.33 and 0.61 Å, respectively, for the well-ordered regions (residues 8−58) of the wild-type (Figure 2A) and R24H mutant (Figure 2B) homeodomains.

The well-ordered regions are composed primarily of three helices spanning residues 10−22, 28−38, and 42−58 (helices α1, α2, and α3, respectively). The helices are connected via two short loops, L1 and L2. The eight conserved hydrophobic residues in combination with P26 and I34 form the protein core, and helices α1 and α2 run roughly parallel to each other and perpendicular to α3. This tertiary structure is representative of the canonical homeodomain fold. An overlay of the average wild-type and R24H mutant Pitx2 homeodomain structures (Figure 2C) indicates that the overall fold is minimally perturbed by the R24H mutation. With respect to the DNA-bound Pitx2 homeodomain complex[24] (Figure 2D), a superposition with the well-structured portion of the free (wild-type) homeodomain reveals a close alignment, with a backbone rmsd (as determined by PyMol) of 0.713 Å.

In contrast to the rigid and well-structured protein core, it is clearly evident from the superposition of the 20 structure conformers, as well as the backbone relaxation measurements (vide infra), that the N-terminal arm (residues 1−9) samples a broad conformational space in the absence of a binding partner. In the presence of the TAATCC consensus DNA, the N-terminal arm binds in the minor groove of DNA (Figure 2D) and becomes more rigid as specific interactions between the N-terminal arginines and the DNA bases are formed.[24]

The arginine at position 24 is solvent-exposed and does not exhibit any long-range NOE constraints in the absence of DNA. However, in the presence of its consensus TAATCC DNA binding site, R24 is oriented in the proximity of the phosphate backbone and likely makes a nonspecific electrostatic contact. A histidine in this position (R24H) could make a similar contact, depending on the pK_a of its cyclic imidazole side chain.

NMR Histidine pH Titration. The typical arginine side chain pK_a is ∼12.5, whereas the pK_a of a histidine side chain is typically much lower (∼6.0). To address a possible charge effect of the arginine to histidine mutation, we recorded 2D ^{1}H−^{15}N HSQC spectra of a uniformly ^{15}N-labeled R24H mutant Pitx2 homeodomain between pH 4.0 and 8.0 in 0.5 pH unit increments. In the spectra recorded at pH <7.5, four cross-peaks corresponding to the $H^{\varepsilon1}$−$N^{\delta1}$, $H^{\varepsilon1}$−$N^{\varepsilon2}$, $H^{\delta2}$−$N^{\varepsilon2}$, and $H^{\delta2}$−$N^{\delta1}$ resonances were observed for both H7 and H24 (Figure 3A). At pH ≥7.5, only three cross-peaks corresponding to the H7 $H^{\varepsilon1}$−$N^{\delta1}$, $H^{\varepsilon1}$−$N^{\varepsilon2}$, and $H^{\delta2}$−$N^{\varepsilon2}$ resonances were observed. Figure 3B shows the pH titration curves for the $N^{\delta1}$ chemical shifts. pK_a values of 6.57 ± 0.04 (H7) and 6.76 ± 0.08 (H24) were calculated by fitting the pH titration data to the Henderson−Hasselbalch equation. Thus, at an experimental pH of 7.0, the histidine side chains are approximately 63 and 73% deprotonated for H24 and H7, respectively.

^{15}N Backbone Relaxation Analysis. ^{15}N R_1 and R_2 relaxation parameters were determined at proton frequencies of 600 and 400 MHz and {^{1}H}−^{15}N heteronuclear NOE data at 600 MHz, at a temperature of 295 K, to compare the conformational flexibility of the wild-type and R24H mutant Pitx2 homeodomains. The relaxation data for the wild-type Pitx2 homeodomain were collected on a 0.5 mM sample. For

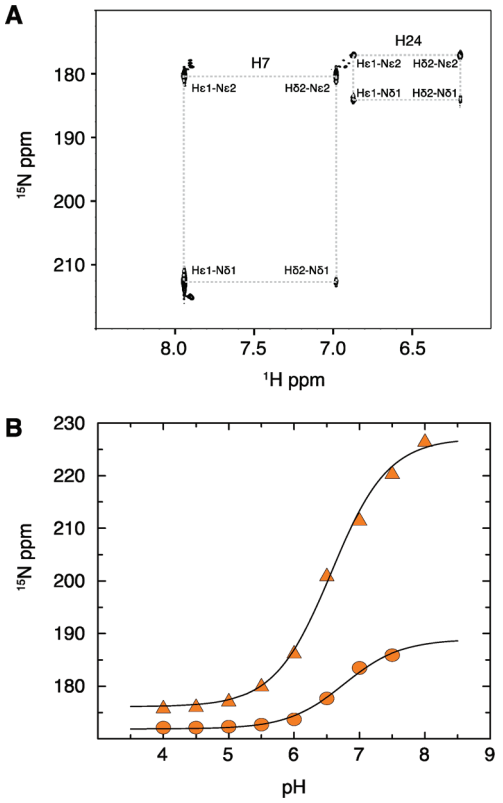

Figure 3. NMR titration of the histidine side chain. (A) A pH 7.0 snapshot of a long-range ^{1}H−^{15}N HSQC experiment for detecting the pH-dependent protonation of the two histidine side chains in the R24H Pitx2 homeodomain mutant. (B) Chemical shift titration curves of the ^{15}N chemical shifts of the histidine $N^{\delta1}$ side chain resonances with fits to eq 1. Triangles correspond to data for H7 and circles to data for H24.

the R24H mutant homeodomain, the R_1 and R_2 relaxation data were collected for four samples, with sample concentrations of 1, 0.5, 0.25, and 0.125 mM. Following extraction of the individual relaxation parameters (presented graphically in Figure 1 of the Supporting Information), the complete data sets at 0.5 mM were subjected to Modelfree analysis[72] for the determination of S^2 generalized order parameters (Figure 4). The backbone ^{15}N order parameters, a measure that distinguishes ordered from flexible regions in a protein, can range from a value of 1, indicative of completely restricted internal motion (on the picosecond to nanosecond time scale), to a value of 0, indicative of completely unrestricted motion. The relaxation data were fit using an isotropic and an axially symmetric diffusion tensor for both the wild-type and R24H mutant Pitx2 homeodomains, and for both homeodomains, χ^2 analysis led to the selection of the symmetric diffusion model. This data analysis yielded values of 7.9 and 7.5 ns for the overall rotational correlation times and values for rotational anisotropy D_r of 0.78 and 0.83 for the wild-type and R24H mutant homeodomains, respectively. The values determined for the overall rotational correlation times are larger than one would expect for homeodomain monomers tumbling freely in solution, thus indicating the presence of some degree of self-association, presumably a monomer−dimer equilibrium. This observation is corroborated by the concentration dependence of the ^{15}N R_2 rate constants (Figure 1 of the Supporting Information). The self-association appears to be relatively weak

dx.doi.org/10.1021/bi201639x | Biochemistry 2012, 51, 665−676

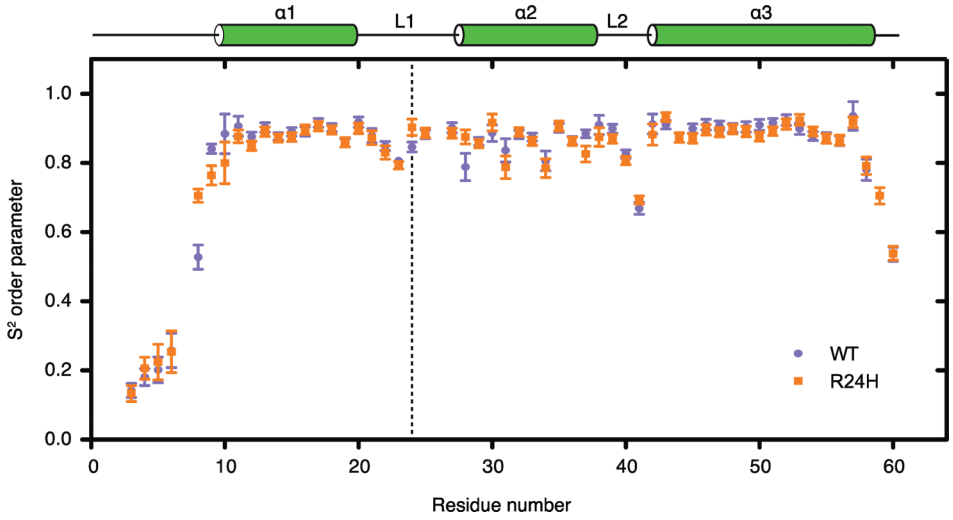

Figure 4. S^2 generalized order parameters for the wild-type (●) and R24H mutant (■) Pitx2 homeodomains. The N-terminal arm is highly flexible in the absence of a DNA binding partner. The three helices exhibit average S^2 values of ~0.85, suggesting an only limited degree of internal motion. The connecting loop regions L1 and L2 generally have lower S^2 values indicative of increased picosecond to nanosecond internal motion in these regions. Similar to the N-terminus, the C-terminus is highly mobile [including the six-amino acid artificial tail (data not shown)]. The vertical dashed line indicates the position of residue 24.

and nonspecific, as no significant changes in amide ^{1}H and ^{15}N chemical shifts were observed in the concentration series of data. Although S^2 values can be overestimated for proteins that self-associate, previous experimental studies have found increases in S^2 that were not dramatic.[73,74] In the analysis presented below, we limit ourselves to qualitative rather than detailed quantitative comparisons regarding the S^2 values of the Pitx2 homeodomains.

The generalized order parameter S^2, heteronuclear NOE, and R_2 data all suggest that the N-terminal arm is highly flexible in the absence of DNA (Figure 4 and Figure 1 of the Supporting Information). This finding is also reflected in our solution structures that lack any long-range structural restraints in the first nine residues and is consistent with previous reports about the backbone dynamics of the vnd/NK-2 and TTF-1 homeodomains.[75,76] In the presence of its consensus DNA, the N-terminal arm binds in the minor groove of DNA and loses some of its mobility characteristics.[21,24] This change in the dynamic nature of the N-terminal arm is thought to contribute significantly to the process of specific DNA binding by the homeodomain motif.[77−80] In addition, loop regions L1 and L2 connecting α1 with α2 and α2 with α3 display a higher degree of motion than the rest of the protein, as indicated by the S^2, NOE, R_1, and R_2 data. This effect, especially in the L2 region, is more striking than in previous studies of other homeodomains[75,76] and may allow the L1 and L2 regions to serve as hinges for the homeodomain to adjust the positions of its helices relative to each other. The core fold (α1, α2, and α3) of the Pitx2 homeodomain, by contrast, is relatively restricted, independent of a DNA binding event.

In comparison to the wild-type data, around the point of the R24H mutation the dynamic behavior is generally little changed as measured by the S^2 values. Residue H24 is modestly more restricted than the wild-type R24 residue. Residue M28 is also modestly more restricted in the R24H mutant than in the wild-type homeodomain. The immediately downstream residues Y25 and D27 (P26 cannot be observed because of the unique nature of the proline cyclic side chain) and upstream residues N23 and R22 also exhibit a comparable degree of internal motion, suggesting that the local dynamic environment is not significantly perturbed by this mutation. Residues F8, T9, and W37 display S^2 values that differ between the wild-type and mutant proteins. In these cases, different motional models were selected for the wild-type versus mutant homeodomains, and thus, the possibility that the observed differences arise due to model selection bias in the calculation of the generalized order parameters for these residues exists. Compared to helices 1 and 3, helix 2 exhibits somewhat greater variability of the S^2 values along the helix, for both wild-type and mutant proteins. Also in common between the two isoforms is an increase in flexibility toward the end of helix 3. This observation likely explains the observed increase in the level of disorder in this region of the structures shown in Figure 2. Data for residue R59 in the wild-type homeodomain are absent from Figure 4 as none of the motional models that were considered provided an adequate fit of the relaxation data. The apparent increased level of disorder at the C-terminal end of helix 3 for the wild-type homeodomain versus the R24H mutant is likely due to the increased number of structural constraints that were obtained for the mutant (Table 1), as the relaxation data do not indicate significant differences in dynamic disorder.

With regard to slower motional processes on the microsecond to millisecond time scale, only residue T38 at the beginning of loop 2 appears to be significantly affected as measured by the R_{ex} term of the Modelfree data analysis, and the wild-type and R24H homeodomains exhibit similar values (3.5 ± 0.6 and 4.6 ± 0.5 Hz, respectively). There is strong evidence of even slower motions for most of the N-terminal arm residues, again for both homeodomains, as judged by the significantly weakened intensities for these residues in the NMR spectra (Figure 2 of the Supporting Information).

Stability of the Free and DNA-Bound Homeodomain. To address whether the R24H mutation and the resultant changes in helix orientation have an impact on protein stability, we performed CD spectroscopy on the free and DNA-bound forms of the Pitx2 homeodomains. The solution structures confirmed that both isoforms possess the typical homeodomain fold, yet the thermal denaturation profile reveals that the R24H

dx.doi.org/10.1021/bi201639x | *Biochemistry* 2012, 51, 665−676

mutant is significantly less stable (T_m = 37.8 °C) than the wild-type homeodomain (T_m = 42 °C) (Figure 5). The wild-type T_m is comparable to that of the K-50 class Bicoid homeodomain (44 °C)[81] and those of many other characterized homeodomains.[81−83] Both isoforms display a two-state folding transition that is stabilized by binding to the TAATCC consensus DNA site (Figure 5). Interestingly, the degree of stabilization arising from binding DNA appears to be independent of the mutation, 16.4 and 16.5 °C for the mutant and wild-type proteins, respectively. This same observation holds true for a nonconsensus DNA sequence that stabilizes both homeodomain isoforms by ∼10 °C (data not shown). The functional consequences of the reduced thermal stability of the R24H mutant are currently unknown; it is possible that this reduction could lead to more rapid degradation of the mutant in vivo.

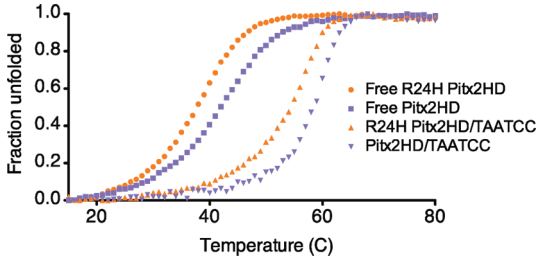

Figure 5. Thermal unfolding profiles of the Pitx2 homeodomain. Unfolded fractions of wild-type and R24H Pitx2 homeodomains plotted as a function of temperature: wild type (■) and R24H (●) for the DNA-free form and wild type (▼) and R24H (▲) for the TAATCC-bound form. The apparent T_m values were 42.0, 37.8, 58.5, and 54.2 °C for the wild-type free, R24H free, wild type−TAATCC, and R24H−TAATCC forms, respectively.

Thermodynamics of Pitx2 Homeodomain−Consensus DNA Binding. To investigate the thermodynamic parameters involved in the formation of the Pitx2 homeodomain−consensus DNA complex, we performed isothermal titration calorimetry (ITC). All ITC experiments were performed with our purified recombinant protein in the reaction chamber and titration in duplex TAATCC consensus DNA. As shown in Table 2, the interactions of the wild-type and R24H mutant Pitx2 homeodomains with the consensus DNA duplex are exothermic and exhibit 1:1 stoichiometry. The reactions are enthalpically driven with a significant entropic contribution. Interestingly, the mutant exhibits a greater entropic contribution that makes the interaction more favorable under the conditions studied. At 25 °C in the presence of 50 mM NaH_2PO_4 and 150 mM NaCl (pH 7.0), the dissociation constants (K_d) for the complexes are ∼26 nM for the R24H mutant and ∼66 nM for the wild-type protein (Figure 6). These values are well within the typical range found for DNA-binding proteins and homeodomain complexes in particular.[84−86] Given the strong salt dependence of binding for the K-50 class homeodomains (unpublished observations) as well as for homeodomains in general,[84] the association and dissociation parameters vary greatly depending on buffer composition, and it is not surprising that previous gel shift experiments with a lower-salt buffer yielded lower K_d values.[24] In the absence of a high-resolution structure of a complex of the R24H mutant homeodomain with the consensus DNA sequence, we can only speculate about the physical origin of the higher affinity of the R24H mutant for the DNA. One possibility is that the R24H mutation introduces small rearrangements of nearby side chains that lead to more optimal interactions with the DNA.

Pitx2c Luciferase Reporter. To improve our understanding of the impact of the R24H mutation in the context of the full-length protein, we transiently transfected HEK293 cells with an expression plasmid for human Pitx2c (wild-type or R24H mutant) and a luciferase reporter under the control of Pitx2c target gene *CCND2* (Figure 7). Both wild-type and R24H mutant Pitx2c proteins are expressed at comparable protein levels. Compared to that of the wild-type protein, the transactivation response of the R24H mutant is approximately 25% weaker, indicating that the mutation does not entirely abolish the transactivation response as in the case of other Pitx2 homeodomain mutations.[8,46,89]

■ DISCUSSION

Solution Structures. Overall, the Pitx2 homeodomain fold represents a typical homeodomain motif, with three helical regions in a compactly folded structure, and a flexible N-terminal tail. No major structural differences were observed between the wild type and R24H mutant. This observation is consistent with the fact that the R24H mutation does not lead to severe dysfunction of Pitx2. In contrast, a $^1H-^{15}N$ HSQC 2D NMR spectrum of the V45L mutant of Pitx2 (Figure 3 of the Supporting Information), which is also a clinically observed mutation, indicates a significant perturbation of the stable fold that is consistent with the weakened DNA binding that has been reported for this mutant.[44] Unlike V45, R24 is not part of the hydrophobic core of the homeodomain, and thus, its mutation leads to more subtle effects on the structure.

Functional Effect of the R24H Mutation. The experimentally determined pK_a value of 6.76 for the R24H mutant differs significantly from the typical arginine pK_a of 12.5. In a biological environment, the arginine is likely charged at all times whereas the histidine residue will exist in a protonated−deprotonated equilibrium that may range from ∼73% deprotonated at a cytosolic pH of 7.2 to ∼90% deprotonated at a nuclear pH of 7.7.[87] The absence of a base-specific contact of R24 in the Pitx2 homeodomain−DNA complex suggests that the charge of the arginine is not needed to confer DNA binding specificity. Indeed, our ITC experiments at pH 7.0 indicate that the mutant has a 2-fold higher binding affinity than the wild-type homeodomain. The observation in our circular dichroism experiments that addition of different target DNA sequences stabilized wild-type and mutant homeodomains to identical degrees further implies that a positive side chain charge at position 24 is not imperative to confer DNA binding specificity. In the absence of an R24H Pitx2 homeodomain−DNA complex structure, our results

Table 2. ITC Measurements of Pitx2 Homeodomain−DNA Complexes

	K (M^{-1})	K_d (nM)	ΔG (kcal/mol)	$\Delta H°$ (kcal/mol)	$-T\Delta S°$ (kcal/mol)
WT Pitx2−TAATCC	(1.51 ± 0.29) × 10^7	66	−9.84 ± 0.27	−7.91 ± 0.17	−1.93 ± 0.10
R24H Pitx2−TAATCC	(3.79 ± 0.37) × 10^7	26	−10.32 ± 0.12	−7.53 ± 0.30	−2.79 ± 0.36

dx.doi.org/10.1021/bi201639x | *Biochemistry* 2012, 51, 665−676

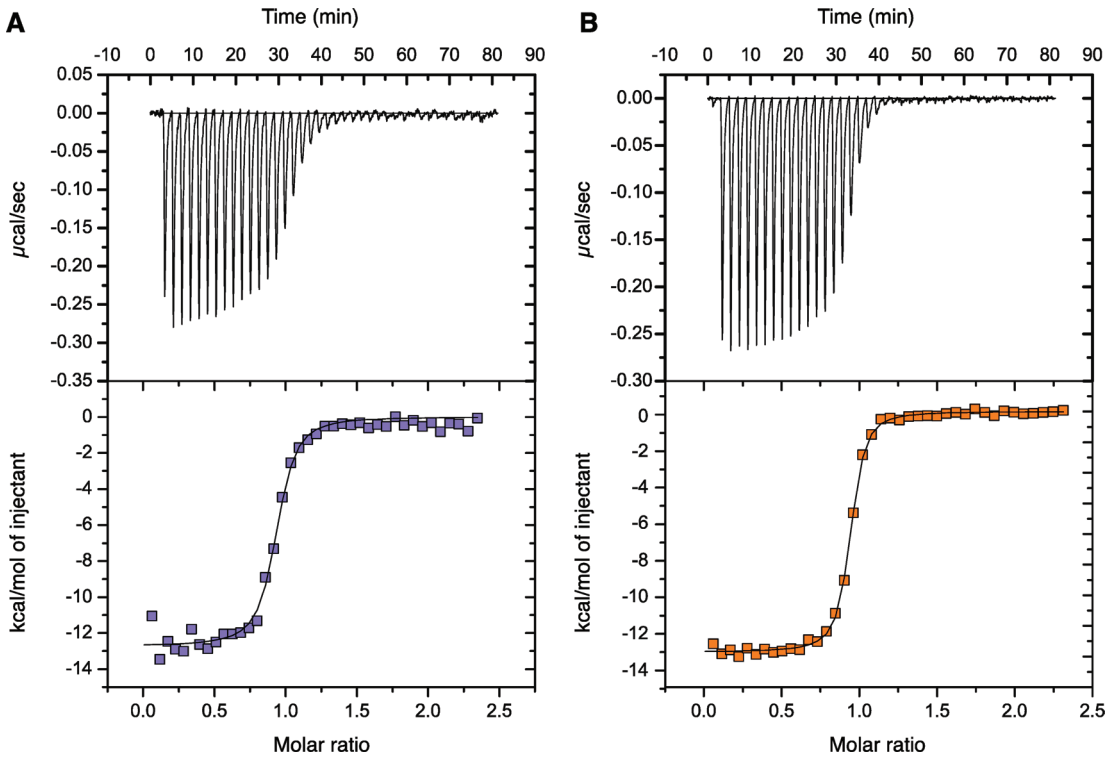

Figure 6. ITC binding data for the Pitx2 homedomain−consensus DNA interaction. (A) A representative isothermal titration of the wild-type Pitx2 homeodomain with TAATCC duplex DNA at 25 °C. (B) A representative isothermal titration of the R24H Pitx2 homeodomain with TAATCC duplex DNA at 25 °C displaying ∼2-fold higher binding affinity.

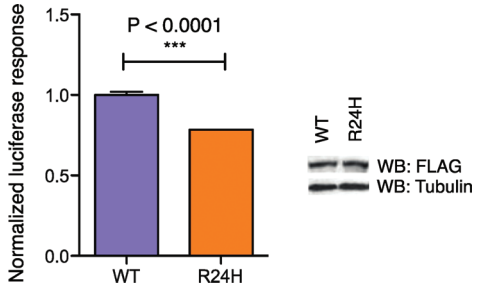

Figure 7. Response of the luciferase reporter to Pitx2 expression in HEK293 cells. A cyclin D2 luciferase reporter was transiently transfected with either full-length wild-type Pitx2c or full-length protein harboring the R24H mutation in the homeodomain. Data represent means ± the standard error of the mean. Western blot analysis confirms that mutant protein is expressed at levels comparable to that of the wild-type protein.

suggest that the lost charge does not impair DNA binding activity. In fact, the Pitx2 R24H solution structure and the experimentally determined histidine pK_a (which closely mimics the reported pK_a value of 6.9 for a solvent-exposed imidazole ring in a Gly-His-Gly model peptide[88]) suggest that residue 24 is generally solvent exposed.

L1 and α2 Region as Transactivation Regulators. With very few exceptions, most of the Pitx2 transactivation activity has previously been attributed to its N- and C-termini.[89] Interestingly, two reported exceptions include the T30P and R31H homeodomain mutations at the beginning of α2. These mutations both result in only slightly reduced levels of DNA binding, but defective transactivation activity in the case of the T30P mutation[9,90] and a reduction to 12.5% of the wild-type levels for the R31H mutation.[91] Similar to the R24 and mutant R24H side chains, the T30 side chain lacks long-range contacts with other amino acids within the homeodomain in all of our NMR structures. In contrast, the R31 side chain is observed in long-range contacts with residues F49 and R46 in helix 3. Unlike those of the T30P and R31H mutants, the DNA binding affinity of the R24H mutant is slightly higher and the transactivation activity is not completely ablated. However, the increase in DNA binding affinity and the simultaneous decrease in transactivation activity suggest that R24 is important for transactivation activity, as well.

A prevailing model in the field describes the C-terminal tail of full-length Pitx2 looping back onto the homeodomain and N-terminus to inactivate the protein.[89] As all our homeodomain structures indicate that residues 24, 30, and 31 are solvent-exposed, these residues could potentially be available to make contacts with the N- and C-termini of Pitx2 or other protein binding partners important for transactivation. The described mutations in L1 or α2 may cause Pitx2 to effectively displace its C-terminal tail, allowing for DNA binding, but not effective transactivation. The fact that most other residues in the vicinity, with the exception of P26, extend away from the homeodomain core and the altered dynamic behavior of the L1 region in the R24H mutant may further imply that this region is involved in intra- or intermolecular protein−protein interactions. Pitx2 is known to interact with other proteins, such as PAWR[92] and the Wnt/DvI/β-catenin pathway,[15] but to the best of our knowledge, the role of R24 in such interactions has not been determined. However, it is well established that residues in loop L1 have important functional consequences in homeodomains.[93]

Dynamic Nature of the Pitx2 Homeodomain. Measurement of ^{15}N backbone relaxation rates provides detailed information about molecular motion on the picosecond to

dx.doi.org/10.1021/bi201639x | *Biochemistry* 2012, 51, 665−676

nanosecond and microsecond to millisecond time scales. A disordered state, such as that described above for the N-terminal arm of the homeodomain, or motions on the slower microsecond to millisecond time scale often correlate to regions involved in protein function, including protein−protein and protein−DNA interactions.[94,95] In addition to the characterized picosecond to nanosecond motion, we have evidence that the N-terminal arm undergoes more complex motion on the microsecond to millisecond time scale. A comparison of the intensities of the amide backbone resonances[96] of the N-terminal arm with the resonances of the artificial C-terminal tail (Figure 2 of the Supporting Information) indicates strong peaks with narrow line widths for the C-terminal tail residues, but a very heterogeneous distribution for the N-terminal arm. Such resonance broadening, especially for residues 1 and 7, is the result of slower motions and warrants further examination to improve our understanding of the dynamic nature of the N-terminal arm and its role in DNA and protein recognition and binding.

■ ASSOCIATED CONTENT

Supporting Information

Figures showing R_1, R_2, and NOE ^{15}N relaxation parameters (Figure 1) and line broadening for residues in the N-terminal arm (Figure 2) for the wild-type Pitx2 homeodomain and the R24H mutant and two-dimensional $^{1}H-^{15}N$ HSQC spectra (Figure S3) for the wild-type, R24H mutant, and V45L mutant Pitx2 homeodomains. This material is available free of charge via the Internet at http://pubs.acs.org.

■ AUTHOR INFORMATION

Corresponding Author

*Phone: (513) 558-0066. Fax: (513) 558-8474. E-mail: mark.rance@uc.edu.

Funding

This project was supported by National Institutes of Health Grants GM063855 to M.R., RR19077 and RR027755 to the University of Cincinnati College of Medicine Nuclear Magnetic Resonance facility, ES007250 and AI055406 to D.J.K., and HL007382 to J.M.B.-T. and an American Heart Association Fellowship and Fight for Sight Summer Student Fellowship to T.D.

■ ACKNOWLEDGMENTS

We thank Jun Ma (Cincinnati Children's Hospital Research Foundation, Cincinnati, OH) for providing the original Pitx2 homeodomain plasmid, Al Combs for subsequent construct optimization, and Guo-Zhang Zhu (Marshall University) for generously supplying the PITX2c vectors. We thank Walter Chazin and Jarrod Smith (Vanderbilt University, Nashville, TN) for kindly providing FINDFAM. We thank Andrew Herr, Rhett Kovall, and Paul Rosevear for helpful comments.

■ ABBREVIATIONS

TEV, tobacco etch virus; PBS, phosphate-buffered saline; NMR, nuclear magnetic resonance; NOE, nuclear Overhauser effect; CPMG, Carr−Purcell−Meiboom−Gill; CD, circular dichroism; ITC, isothermal titration calorimetry; NOESY, nuclear Overhauser effect spectroscopy; HSQC, heteronuclear single-quantum correlation; PDB, Protein Data Bank.

■ REFERENCES

(1) Logan, M., Pagan-Westphal, S. M., Smith, D. M., Paganessi, L., and Tabin, C. J. (1998) The transcription factor Pitx2 mediates situs-specific morphogenesis in response to left-right asymmetric signals. *Cell 94*, 307−317.

(2) Ryan, A. K., Blumberg, B., Rodriguez-Esteban, C., Yonei-Tamura, S., Tamura, K., Tsukui, T., de la Pena, J., Sabbagh, W., Greenwald, J., Choe, S., Norris, D. P., Robertson, E. J., Evans, R. M., Rosenfeld, M. G., and Izpisua Belmonte, J. C. (1998) Pitx2 determines left-right asymmetry of internal organs in vertebrates. *Nature 394*, 545−551.

(3) Campione, M., Steinbeisser, H., Schweickert, A., Deissler, K., van Bebber, F., Lowe, L. A., Nowotschin, S., Viebahn, C., Haffter, P., Kuehn, M. R., and Blum, M. (1999) The homeobox gene Pitx2: Mediator of asymmetric left-right signaling in vertebrate heart and gut looping. *Development 126*, 1225−1234.

(4) Campione, M., Ros, M. A., Icardo, J. M., Piedra, E., Christoffels, V. M., Schweickert, A., Blum, M., Franco, D., and Moorman, A. F. (2001) Pitx2 expression defines a left cardiac lineage of cells: Evidence for atrial and ventricular molecular isomerism in the iv/iv mice. *Dev. Biol. 231*, 252−264.

(5) Yoshioka, H., Meno, C., Koshiba, K., Sugihara, M., Itoh, H., Ishimaru, Y., Inoue, T., Ohuchi, H., Semina, E. V., Murray, J. C., Hamada, H., and Noji, S. (1998) Pitx2, a bicoid-type homeobox gene, is involved in a lefty-signaling pathway in determination of left-right asymmetry. *Cell 94*, 299−305.

(6) Su, A. I., Wiltshire, T., Batalov, S., Lapp, H., Ching, K. A., Block, D., Zhang, J., Soden, R., Hayakawa, M., Kreiman, G., Cooke, M. P., Walker, J. R., and Hogenesch, J. B. (2004) A gene atlas of the mouse and human protein-encoding transcriptomes. *Proc. Natl. Acad. Sci. U.S.A. 101*, 6062−6067.

(7) Sjodal, M., and Gunhaga, L. (2008) Expression patterns of Shh, Ptc2, Raldh3, Pitx2, Isl1, Lim3 and Pax6 in the developing chick hypophyseal placode and Rathke's pouch. *Gene Expression Patterns 8*, 481−485.

(8) Semina, E. V., Reiter, R., Leysens, N. J., Alward, W. L., Small, K. W., Datson, N. A., Siegel-Bartelt, J., Bierke-Nelson, D., Bitoun, P., Zabel, B. U., Carey, J. C., and Murray, J. C. (1996) Cloning and characterization of a novel bicoid-related homeobox transcription factor gene, RIEG, involved in Rieger syndrome. *Nat. Genet. 14*, 392−399.

(9) Saadi, I., Semina, E. V., Amendt, B. A., Harris, D. J., Murphy, K. P., Murray, J. C., and Russo, A. F. (2001) Identification of a dominant negative homeodomain mutation in Rieger syndrome. *J. Biol. Chem. 276*, 23034−23041.

(10) Lin, C. R., Kioussi, C., O'Connell, S., Briata, P., Szeto, D., Liu, F., Izpisua-Belmonte, J. C., and Rosenfeld, M. G. (1999) Pitx2 regulates lung asymmetry, cardiac positioning and pituitary and tooth morphogenesis. *Nature 401*, 279−282.

(11) Alward, W. L., Semina, E. V., Kalenak, J. W., Heon, E., Sheth, B. P., Stone, E. M., and Murray, J. C. (1998) Autosomal dominant iris hypoplasia is caused by a mutation in the Rieger syndrome (RIEG/PITX2) gene. *Am. J. Ophthalmol. 125*, 98−100.

(12) Kulak, S. C., Kozlowski, K., Semina, E. V., Pearce, W. G., and Walter, M. A. (1998) Mutation in the RIEG1 gene in patients with iridogoniodysgenesis syndrome. *Hum. Mol. Genet. 7*, 1113−1117.

(13) Tumer, Z., and Bach-Holm, D. (2009) Axenfeld-Rieger syndrome and spectrum of PITX2 and FOXC1 mutations. *Eur. J. Hum. Genet. 17*, 1527−1539.

(14) Kitamura, K., Miura, H., Miyagawa-Tomita, S., Yanazawa, M., Katoh-Fukui, Y., Suzuki, R., Ohuchi, H., Suehiro, A., Motegi, Y., Nakahara, Y., Kondo, S., and Yokoyama, M. (1999) Mouse Pitx2 deficiency leads to anomalies of the ventral body wall, heart, extra- and periocular mesoderm and right pulmonary isomerism. *Development 126*, 5749−5758.

(15) Kioussi, C., Briata, P., Baek, S. H., Rose, D. W., Hamblet, N. S., Herman, T., Ohgi, K. A., Lin, C., Gleiberman, A., Wang, J., Brault, V., Ruiz-Lozano, P., Nguyen, H. D., Kemler, R., Glass, C. K., Wynshaw-Boris, A., and Rosenfeld, M. G. (2002) Identification of a Wnt/Dvl/β-

Catenin → Pitx2 pathway mediating cell-type-specific proliferation during development. *Cell 111*, 673−685.
(16) Vadlamudi, U., Espinoza, H. M., Ganga, M., Martin, D. M., Liu, X., Engelhardt, J. F., and Amendt, B. A. (2005) PITX2, β-catenin and LEF-1 interact to synergistically regulate the LEF-1 promoter. *J. Cell Sci. 118*, 1129−1137.
(17) Derynck, R., Zhang, Y., and Feng, X. H. (1998) Smads: Transcriptional activators of TGF-β responses. *Cell 95*, 737−740.
(18) Xiao, H., and Zhang, Y. Y. (2008) Understanding the role of transforming growth factor-β signalling in the heart: Overview of studies using genetic mouse models. *Clin. Exp. Pharmacol. Physiol. 35*, 335−341.
(19) Glasgow, E., and Mishra, L. (2008) Transforming growth factor-β signaling and ubiquitinators in cancer. *Endocr.-Relat. Cancer 15*, 59−72.
(20) Suszko, M. I., Antenos, M., Balkin, D. M., and Woodruff, T. K. (2008) Smad3 and Pitx2 cooperate in stimulation of FSHβ gene transcription. *Mol. Cell. Endocrinol. 281*, 27−36.
(21) Baird-Titus, J. M., Clark-Baldwin, K., Dave, V., Caperelli, C. A., Ma, J., and Rance, M. (2006) The solution structure of the native K50 Bicoid homeodomain bound to the consensus TAATCC DNA-binding site. *J. Mol. Biol. 356*, 1137−1151.
(22) Billeter, M., Guntert, P., Luginbuhl, P., and Wuthrich, K. (1996) Hydration and DNA recognition by homeodomains. *Cell 85*, 1057−1065.
(23) Scott, M. P., Tamkun, J. W., and Hartzell, G. W. III (1989) The structure and function of the homeodomain. *Biochim. Biophys. Acta 989*, 25−48.
(24) Chaney, B. A., Clark-Baldwin, K., Dave, V., Ma, J., and Rance, M. (2005) Solution structure of the K50 class homeodomain PITX2 bound to DNA and implications for mutations that cause Rieger syndrome. *Biochemistry 44*, 7497−7511.
(25) Ades, S. E., and Sauer, R. T. (1994) Differential DNA-binding specificity of the engrailed homeodomain: The role of residue 50. *Biochemistry 33*, 9187−9194.
(26) Billeter, M., Qian, Y. Q., Otting, G., Muller, M., Gehring, W., and Wuthrich, K. (1993) Determination of the nuclear magnetic resonance solution structure of an Antennapedia homeodomain-DNA complex. *J. Mol. Biol. 234*, 1084−1093.
(27) Fraenkel, E., Rould, M. A., Chambers, K. A., and Pabo, C. O. (1998) Engrailed homeodomain-DNA complex at 2.2 Å resolution: A detailed view of the interface and comparison with other engrailed structures. *J. Mol. Biol. 284*, 351−361.
(28) Gruschus, J. M., Tsao, D. H., Wang, L. H., Nirenberg, M., and Ferretti, J. A. (1999) The three-dimensional structure of the vnd/NK-2 homeodomain-DNA complex by NMR spectroscopy. *J. Mol. Biol. 289*, 529−545.
(29) Hirsch, J. A., and Aggarwal, A. K. (1995) Structure of the even-skipped homeodomain complexed to AT-rich DNA: New perspectives on homeodomain specificity. *EMBO J. 14*, 6280−6291.
(30) Hovde, S., Abate-Shen, C., and Geiger, J. H. (2001) Crystal structure of the Msx-1 homeodomain/DNA complex. *Biochemistry 40*, 12013−12021.
(31) Joshi, R., Passner, J. M., Rohs, R., Jain, R., Sosinsky, A., Crickmore, M. A., Jacob, V., Aggarwal, A. K., Honig, B., and Mann, R. S. (2007) Functional specificity of a Hox protein mediated by the recognition of minor groove structure. *Cell 131*, 530−543.
(32) Li, T., Stark, M. R., Johnson, A. D., and Wolberger, C. (1995) Crystal structure of the MATa1/MATα2 homeodomain heterodimer bound to DNA. *Science 270*, 262−269.
(33) Longo, A., Guanga, G. P., and Rose, R. B. (2007) Structural basis for induced fit mechanisms in DNA recognition by the Pdx1 homeodomain. *Biochemistry 46*, 2948−2957.
(34) Passner, J. M., Ryoo, H. D., Shen, L., Mann, R. S., and Aggarwal, A. K. (1999) Structure of a DNA-bound Ultrabithorax-Extradenticle homeodomain complex. *Nature 397*, 714−719.
(35) Piper, D. E., Batchelor, A. H., Chang, C. P., Cleary, M. L., and Wolberger, C. (1999) Structure of a HoxB1-Pbx1 heterodimer bound to DNA: Role of the hexapeptide and a fourth homeodomain helix in complex formation. *Cell 96*, 587−597.
(36) Wilson, D., Sheng, G., Lecuit, T., Dostatni, N., and Desplan, C. (1993) Cooperative dimerization of paired class homeo domains on DNA. *Genes Dev. 7*, 2120−2134.
(37) Wilson, D. S., Guenther, B., Desplan, C., and Kuriyan, J. (1995) High resolution crystal structure of a paired (Pax) class cooperative homeodomain dimer on DNA. *Cell 82*, 709−719.
(38) Wilson, D. S., Sheng, G., Jun, S., and Desplan, C. (1996) Conservation and diversification in homeodomain-DNA interactions: A comparative genetic analysis. *Proc. Natl. Acad. Sci. U.S.A. 93*, 6886−6891.
(39) Wolberger, C., Vershon, A. K., Liu, B., Johnson, A. D., and Pabo, C. O. (1991) Crystal structure of a MATα2 homeodomain-operator complex suggests a general model for homeodomain-DNA interactions. *Cell 67*, 517−528.
(40) Dave, V., Zhao, C., Yang, F., Tung, C. S., and Ma, J. (2000) Reprogrammable recognition codes in bicoid homeodomain-DNA interaction. *Mol. Cell. Biol. 20*, 7673−7684.
(41) Xia, K., Wu, L., Liu, X., Xi, X., Liang, D., Zheng, D., Cai, F., Pan, Q., Long, Z., Dai, H., Hu, Z., Tang, B., Zhang, Z., and Xia, J. (2004) Mutation in PITX2 is associated with ring dermoid of the cornea. *J. Med. Genet. 41*, e129.
(42) Phillips, J. C. (2002) Four novel mutations in the PITX2 gene in patients with Axenfeld-Rieger syndrome. *Ophthalmic Res. 34*, 324−326.
(43) Weisschuh, N., Dressler, P., Schuettauf, F., Wolf, C., Wissinger, B., and Gramer, E. (2006) Novel mutations of FOXC1 and PITX2 in patients with Axenfeld-Rieger malformations. *Invest. Ophthalmol. Visual Sci. 47*, 3846−3852.
(44) Priston, M., Kozlowski, K., Gill, D., Letwin, K., Buys, Y., Levin, A. V., Walter, M. A., and Heon, E. (2001) Functional analyses of two newly identified PITX2 mutants reveal a novel molecular mechanism for Axenfeld-Rieger syndrome. *Hum. Mol. Genet. 10*, 1631−1638.
(45) Li, D., Zhu, Q., Lin, H., Zhou, N., and Qi, Y. (2008) A novel PITX2 mutation in a Chinese family with Axenfeld-Rieger syndrome. *Mol. Vision 14*, 2205−2210.
(46) Perveen, R., Lloyd, I. C., Clayton-Smith, J., Churchill, A., van Heyningen, V., Hanson, I., Taylor, D., McKeown, C., Super, M., Kerr, B., Winter, R., and Black, G. C. (2000) Phenotypic variability and asymmetry of Rieger syndrome associated with PITX2 mutations. *Invest. Ophthalmol. Visual Sci. 41*, 2456−2460.
(47) Idrees, F., Bloch-Zupan, A., Free, S. L., Vaideanu, D., Thompson, P. J., Ashley, P., Brice, G., Rutland, P., Bitner-Glindzicz, M., Khaw, P. T., Fraser, S., Sisodiya, S. M., and Sowden, J. C. (2006) A novel homeobox mutation in the PITX2 gene in a family with Axenfeld-Rieger syndrome associated with brain, ocular, and dental phenotypes. *Am. J. Med. Genet., Part B 141*, 184−191.
(48) Footz, T., Idrees, F., Acharya, M., Kozlowski, K., and Walter, M. A. (2009) Analysis of mutations of the PITX2 transcription factor found in patients with Axenfeld-Rieger syndrome. *Invest. Ophthalmol. Visual Sci. 50*, 2599−2606.
(49) Vieira, V., David, G., Roche, O., de la Houssaye, G., Boutboul, S., Arbogast, L., Kobetz, A., Orssaud, C., Camand, O., Schorderet, D. F., Munier, F., Rossi, A., Delezoide, A. L., Marsac, C., Ricquier, D., Dufier, J. L., Menasche, M., and Abitbol, M. (2006) Identification of four new PITX2 gene mutations in patients with Axenfeld-Rieger syndrome. *Mol. Vision 12*, 1448−1460.
(50) Delaglio, F., Grzesiek, S., Vuister, G. W., Zhu, G., Pfeifer, J., and Bax, A. (1995) NMRPipe: A multidimensional spectral processing system based on UNIX pipes. *J. Biomol. NMR 6*, 277−293.
(51) Johnson, B. A. (2004) Using NMRView to visualize and analyze the NMR spectra of macromolecules. *Methods Mol. Biol. 278*, 313−352.
(52) Shen, Y., Delaglio, F., Cornilescu, G., and Bax, A. (2009) TALOS+: A hybrid method for predicting protein backbone torsion angles from NMR chemical shifts. *J. Biomol. NMR 44*, 213−223.

(53) Tsui, V., and Case, D. A. (2000) Theory and applications of the generalized Born solvation model in macromolecular simulations. *Biopolymers 56*, 275−291.
(54) Case, D. A., Cheatham, T. E. III, Darden, T., Gohlke, H., Luo, R., Merz, K. M. Jr., Onufriev, A., Simmerling, C., Wang, B., and Woods, R. J. (2005) The Amber biomolecular simulation programs. *J. Comput. Chem. 26*, 1668−1688.
(55) Xia, B., Tsui, V., Case, D. A., Dyson, H. J., and Wright, P. E. (2002) Comparison of protein solution structures refined by molecular dynamics simulation in vacuum, with a generalized Born model, and with explicit water. *J. Biomol. NMR 22*, 317−331.
(56) Smith, J. A., Gomez-Paloma, L., Case, D. A., and Chazin, W. J. (1996) Molecular dynamics docking driven by NMR-derived restraints to determine the structure of the calicheamicin γ_1^I oligosaccharide domain complexed to duplex DNA. *Magn. Reson. Chem. 34*, S147−S155.
(57) Davis, I. W., Leaver-Fay, A., Chen, V. B., Block, J. N., Kapral, G. J., Wang, X., Murray, L. W., Arendall, W. B. III, Snoeyink, J., Richardson, J. S., and Richardson, D. C. (2007) MolProbity: All-atom contacts and structure validation for proteins and nucleic acids. *Nucleic Acids Res. 35*, W375−W383.
(58) Hass, M. A., Hansen, D. F., Christensen, H. E., Led, J. J., and Kay, L. E. (2008) Characterization of conformational exchange of a histidine side chain: Protonation, rotamerization, and tautomerization of His61 in plastocyanin from *Anabaena variabilis*. *J. Am. Chem. Soc. 130*, 8460−8470.
(59) Farrow, N. A., Muhandiram, R., Singer, A. U., Pascal, S. M., Kay, C. M., Gish, G., Shoelson, S. E., Pawson, T., Forman-Kay, J. D., and Kay, L. E. (1994) Backbone dynamics of a free and phosphopeptide-complexed Src homology 2 domain studied by ^{15}N NMR relaxation. *Biochemistry 33*, 5984−6003.
(60) Skelton, N. J., Palmer, A. G., Akke, M., Kordel, J., Rance, M., and Chazin, W. J. (1993) Practical Aspects of 2-Dimensional Proton-Detected N-15 Spin Relaxation Measurements. *J. Magn. Reson., Ser. B 102*, 253−264.
(61) Wang, A. C., and Bax, A. (1993) Minimizing the Effects of Radiofrequency Heating in Multidimensional NMR Experiments. *J. Biomol. NMR 3*, 715−720.
(62) Yip, G. N. B., and Zuiderweg, E. R. P. (2005) Improvement of duty-cycle heating compensation in NMR spin relaxation experiments. *J. Magn. Reson. 176*, 171−178.
(63) Mulder, F. A., van Tilborg, P. J., Kaptein, R., and Boelens, R. (1999) Microsecond time scale dynamics in the RXR DNA-binding domain from a combination of spin-echo and off-resonance rotating frame relaxation measurements. *J. Biomol. NMR 13*, 275−288.
(64) Palmer, A. G., Rance, M., and Wright, P. E. (1991) Intramolecular Motions of a Zinc Finger DNA-Binding Domain from Xfin Characterized by Proton-Detected Natural Abundance C-12 Heteronuclear NMR-Spectroscopy. *J. Am. Chem. Soc. 113*, 4371−4380.
(65) Ferrage, F., Cowburn, D., and Ghose, R. (2009) Accurate sampling of high-frequency motions in proteins by steady-state ^{15}N-{^{1}H} nuclear Overhauser effect measurements in the presence of cross-correlated relaxation. *J. Am. Chem. Soc. 131*, 6048−6049.
(66) Vugmeyster, L., Trott, O., McKnight, C. J., Raleigh, D. P., and Palmer, A. G. III (2002) Temperature-dependent dynamics of the villin headpiece helical subdomain, an unusually small thermostable protein. *J. Mol. Biol. 320*, 841−854.
(67) Theobald, D. L., and Wuttke, D. S. (2006) THESEUS: Maximum likelihood superpositioning and analysis of macromolecular structures. *Bioinformatics 22*, 2171−2172.
(68) Greenfield, N. J. (2006) Using circular dichroism collected as a function of temperature to determine the thermodynamics of protein unfolding and binding interactions. *Nat. Protoc. 1*, 2527−2535.
(69) Campanini, B., Bologna, S., Cannone, F., Chirico, G., Mozzarelli, A., and Bettati, S. (2005) Unfolding of Green Fluorescent Protein mut2 in wet nanoporous silica gels. *Protein Sci. 14*, 1125−1133.
(70) Huang, Y., Guigon, C. J., Fan, J., Cheng, S. Y., and Zhu, G. Z. (2010) Pituitary homeobox 2 (PITX2) promotes thyroid carcinogenesis by activation of cyclin D2. *Cell Cycle 9*, 1333−1341.
(71) Huang, Y., Huang, K., Boskovic, G., Dementieva, Y., Denvir, J., Primerano, D. A., and Zhu, G. Z. (2009) Proteomic and genomic analysis of PITX2 interacting and regulating networks. *FEBS Lett. 583*, 638−642.
(72) Lipari, G., and Szabo, A. (1982) Model-Free Approach to the Interpretation of Nuclear Magnetic-Resonance Relaxation in Macromolecules. 1. Theory and Range of Validity. *J. Am. Chem. Soc. 104*, 4546−4559.
(73) Baryshnikova, O. K., and Sykes, B. D. (2006) Backbone dynamics of SDF-1α determined by NMR: Interpretation in the presence of monomer-dimer equilibrium. *Protein Sci. 15*, 2568−2578.
(74) Pfuhl, M., Chen, H. A., Kristensen, S. M., and Driscoll, P. C. (1999) NMR exchange broadening arising from specific low affinity protein self-association: analysis of nitrogen-15 nuclear relaxation for rat CD2 domain 1. *J. Biomol. NMR 14*, 307−320.
(75) Gumral, D., Nadalin, L., Corazza, A., Fogolari, F., Damante, G., Viglino, P., and Esposito, G. (2008) Helix mobility and recognition function of the rat thyroid transcription factor 1 homeodomain: Hints from ^{15}N-NMR relaxation studies. *FEBS J. 275*, 435−448.
(76) Fausti, S., Weiler, S., Cuniberti, C., Hwang, K. J., No, K. T., Gruschus, J. M., Perico, A., Nirenberg, M., and Ferretti, J. A. (2001) Backbone dynamics for the wild type and a double H52R/T56W mutant of the vnd/NK-2 homeodomain from *Drosophila melanogaster*. *Biochemistry 40*, 12004−12012.
(77) Berg, O. G., Winter, R. B., and von Hippel, P. H. (1981) Diffusion-driven mechanisms of protein translocation on nucleic acids. 1. Models and theory. *Biochemistry 20*, 6929−6948.
(78) Iwahara, J., and Clore, G. M. (2006) Direct observation of enhanced translocation of a homeodomain between DNA cognate sites by NMR exchange spectroscopy. *J. Am. Chem. Soc. 128*, 404−405.
(79) Iwahara, J., Zweckstetter, M., and Clore, G. M. (2006) NMR structural and kinetic characterization of a homeodomain diffusing and hopping on nonspecific DNA. *Proc. Natl. Acad. Sci. U.S.A. 103*, 15062−15067.
(80) Vuzman, D., Azia, A., and Levy, Y. (2010) Searching DNA via a "Monkey Bar" mechanism: The significance of disordered tails. *J. Mol. Biol. 396*, 674−684.
(81) Subramaniam, V., Jovin, T. M., and Rivera-Pomar, R. V. (2001) Aromatic amino acids are critical for stability of the bicoid homeodomain. *J. Biol. Chem. 276*, 21506−21511.
(82) Damante, G., Tell, G., Leonardi, A., Fogolari, F., Bortolotti, N., Di Lauro, R., and Formisano, S. (1994) Analysis of the conformation and stability of rat TTF-1 homeodomain by circular dichroism. *FEBS Lett. 354*, 293−296.
(83) Otting, G., Qian, Y. Q., Muller, M., Affolter, M., Gehring, W., and Wuthrich, K. (1988) Secondary structure determination for the Antennapedia homeodomain by nuclear magnetic resonance and evidence for a helix-turn-helix motif. *EMBO J. 7*, 4305−4309.
(84) Dragan, A. I., Li, Z., Makeyeva, E. N., Milgotina, E. I., Liu, Y., Crane-Robinson, C., and Privalov, P. L. (2006) Forces driving the binding of homeodomains to DNA. *Biochemistry 45*, 141−151.
(85) Fodor, E., Mack, J. W., Maeng, J. S., Ju, J. H., Lee, H. S., Gruschus, J. M., Ferretti, J. A., and Ginsburg, A. (2005) Cardiac-specific Nkx2.5 homeodomain: Conformational stability and specific DNA binding of Nkx2.5(C56S). *Biochemistry 44*, 12480−12490.
(86) Gonzalez, M., Weiler, S., Ferretti, J. A., and Ginsburg, A. (2001) The vnd/NK-2 homeodomain: Thermodynamics of reversible unfolding and DNA binding for wild-type and with residue replacements H52R and H52R/T56W in helix III. *Biochemistry 40*, 4923−4931.
(87) Seksek, O., and Bolard, J. (1996) Nuclear pH gradient in mammalian cells revealed by laser microspectrofluorimetry. *J. Cell Sci. 109* (Part 1), 257−262.
(88) Markley, J. L. (1975) Observation of Histidine Residues in Proteins by Means of Nuclear Magnetic-Resonance Spectroscopy. *Acc. Chem. Res. 8*, 70−80.
(89) Amendt, B. A. (2005) The molecular and biochemical basis of Axenfeld-Rieger syndrome. In *The Molecular Mechanisms of Axenfeld-*

Rieger Syndrome (Amendt, B. A., Ed.) pp 32−53, Landes Bioscience, New York.
(90) Amendt, B. A., Sutherland, L. B., Semina, E. V., and Russo, A. F. (1998) The molecular basis of Rieger syndrome. Analysis of Pitx2 homeodomain protein activities. *J. Biol. Chem. 273*, 20066−20072.
(91) Kozlowski, K., and Walter, M. A. (2000) Variation in residual PITX2 activity underlies the phenotypic spectrum of anterior segment developmental disorders. *Hum. Mol. Genet. 9*, 2131−2139.
(92) Acharya, M., Lingenfelter, D. J., Huang, L., Gage, P. J., and Walter, M. A. (2009) Human PRKC apoptosis WT1 regulator is a novel PITX2-interacting protein that regulates PITX2 transcriptional activity in ocular cells. *J. Biol. Chem. 284*, 34829−34838.
(93) Chan, S. K., and Mann, R. S. (1993) The segment identity functions of Ultrabithorax are contained within its homeo domain and carboxy-terminal sequences. *Genes Dev. 7*, 796−811.
(94) Frederick, K. K., Marlow, M. S., Valentine, K. G., and Wand, A. J. (2007) Conformational entropy in molecular recognition by proteins. *Nature 448*, 325−329.
(95) Grunberg, R., Nilges, M., and Leckner, J. (2006) Flexibility and conformational entropy in protein-protein binding. *Structure 14*, 683−693.
(96) Doerdelmann, T., Kojetin, D. J., Baird-Titus, J. M., and Rance, M. (2011) ^{1}H, ^{13}C and ^{15}N chemical shift assignments for the human Pitx2 homeodomain and a R24H homeodomain mutant. *Biomol. NMR Assignments 5*, 105−107.